



# KOCAELI JOURNAL OF SCIENCE AND ENGINEERING

## Owner

Prof. Dr. Sadettin HÜLAGÜ - (Kocaeli University)

## Editor in Chief

Prof. Dr. K. Süleyman YİĞİT - (Kocaeli University)

## Associate Editors

Prof. Dr. Murat HOŞÖZ - (Kocaeli University)

Assoc. Prof. Dr. H. Hakan GÜREL - (Kocaeli University)

## Production Editor

Instructor Yusuf YAĞCI - (Kocaeli University)

## Assistant Editors

R. A. Abdurrahman GÜN - (Kocaeli University)

R. A. Alp Eren ŞAHİN - (Kocaeli University)

## Redaction

Lecturer İsmail Hakkı PASLI - (Kocaeli University)

## Secretary

Durmuş İMAT - (Kocaeli University)

## Section Editors

ARIK Mehmet, (Prof. Dr.) - (Özyeğin University, TR)  
AZEVEDO Helena, (Dr.) - (Queen Mary University of London, ENG)  
CASTILLO Oscar, (Prof. Dr.) - (Tijuana Institute of Technology, MEX)  
CİVAN Mihriban, (Asst. Prof. Dr.) - (Kocaeli University, TR)  
ENGİN Tahsin, (Prof. Dr.) - (Sakarya University, TR)  
ERDEMLİ Yunus Emre, (Prof. Dr.) - (Kocaeli University, TR)  
ERTUNÇ H.Metin, (Prof. Dr.) - (Kocaeli University, TR)  
FIĞLALI Nilgün, (Prof. Dr.) - (Kocaeli University, TR)  
GÖKTAŞ Recep Kaya, (Asst. Prof. Dr.) - (Kocaeli University, TR)  
GÜLTEKİN Fatma, (Assoc. Prof. Dr.) - (Karadeniz Technical University, TR)  
GÜRAY Taygun, (Asst. Prof. Dr.) - (Kocaeli University, TR)  
KANDEMİR İlyas, (Assoc. Prof. Dr.) - (Gebze Technical University, TR)  
KASIM Ufuk, (Asst. Prof. Dr.) - (Kocaeli University, TR)  
KILIÇARSLAN Ali, (Prof. Dr.) - (Hitit University, TR)  
ORUÇ Bülent, (Prof. Dr.) - (Kocaeli University, TR)  
ÖZDEMİR Engin, (Prof. Dr.) - (Kocaeli University, TR)  
PEKEY Beyhan, (Assoc. Prof. Dr.) - (Kocaeli University, TR)  
SAYAR Ahmet, (Asst. Prof. Dr.) - (Kocaeli University, TR)  
SAYIN Cenk, (Prof. Dr.) - (Marmara University, TR)  
SINMAZÇELİK Tamer, (Prof. Dr.) - (Kocaeli University, TR)  
SOPIAN Kamaruzzaman, (Prof. Dr.) - (The National University of Malaysia, MAL)  
SOSTAKS Aleksandrs, (Prof. Dr.) - (University of Latvia, LV)  
SÖZEN Adnan, (Prof. Dr.) - (Gazi University, TR)  
STANASEL Iulian, (Assoc. Prof. Dr.) - (University of Oradea, RO)  
ŞAHİN Ahmet Z., (Prof. Dr.) - (KFUPM, SA)

## Advisory Board

AKIN Nilgün, (Prof. Dr.) - (Kocaeli University, TR)  
ALADAĞ Zerrin, (Prof. Dr.) - (Kocaeli University, TR)  
ARI Ayşe Arzu, (Asst. Prof. Dr.) - (Kocaeli University, TR)  
ARICI Müslüm, (Assoc. Prof. Dr.) - (Kocaeli University, TR)  
ATAPEK Hakan, (Assoc. Prof. Dr.) - (Kocaeli University, TR)  
BAYNAL Kasım, (Assoc. Prof. Dr.) - (Kocaeli University, TR)  
ÇANAKCI Mustafa, (Prof. Dr.) - (Kocaeli University, TR)  
ÇEPNİ Murat Selim, (Assoc. Prof. Dr.) - (Kocaeli University, TR)  
ÇETKİN Vildan, (Asst. Prof. Dr.) - (Kocaeli University, TR)  
ÇOBAN Onur, (Asst. Prof. Dr.) - (Kocaeli University, TR)  
ÇOŞKUN Safa Bozkurt, (Prof. Dr.) - (Kocaeli University, TR)  
DEMİR Arif, (Prof. Dr.) - (Kocaeli University, TR)  
EREN Canan Dilek, (Asst. Prof. Dr.) - (Kocaeli University, TR)  
ERGÜL Halim Aytekin, (Assoc. Prof. Dr.) - (Kocaeli University, TR)  
GENÇ Nevim, (Prof. Dr.) - (Kocaeli University, TR)  
GÜNDOĞDU Özcan, (Prof. Dr.) - (Kocaeli University, TR)  
KARAKAŞ Ahmet, (Assoc. Prof. Dr.) - (Kocaeli University, TR)  
KASIM Rezzan, (Prof. Dr.) - (Kocaeli University, TR)  
KİSHALI Emre, (Asst. Prof. Dr.) - (Kocaeli University, TR)  
ÖZER Nil Pembe, (Prof. Dr.) - (Kocaeli University, TR)  
SERTÇELİK Fadime, (Assoc. Prof. Dr.) - (Kocaeli University, TR)  
URHAN Oğuzhan, (Prof. Dr.) - (Kocaeli University, TR)  
YILDIZ Ali Bekir, (Assoc. Prof. Dr.) - (Kocaeli University, TR)  
YILMAZ Mehmet, (Assoc. Prof. Dr.) - (Kocaeli University, TR)  
YİĞİT Halil, (Assoc. Prof. Dr.) - (Kocaeli University, TR)

## Printed By

Kocaeli Üniversitesi - Fen Bilimleri Enstitüsü Umutepe Yerleşkesi 41380, Kocaeli/TURKEY  
Tel: +090 (262) 303 30 32 Fax: +090 (262) 303 30 33 E-mail: kojose@kocaeli.edu.tr



**EDITORIAL PREFACE TO THE FIRST VOLUME OF  
KOCAELI JOURNAL OF SCIENCE AND ENGINEERING**

We are pleased to bring you this inaugural volume of the Kocaeli Journal of Science and Engineering, completed in May 2018 with 4 papers in totally 20 pages.

Kocaeli Journal of Science and Engineering (KOJOSE), abbreviated as Koc. J. Sci. Eng., is an international, multidisciplinary, peer-reviewed, digital, biannual journal containing original research papers and review articles, published by the Graduate School of Natural and Applied Sciences of Kocaeli University.

KOJOSE provides a forum for recent information on research, innovation and development in a wide variety of areas of science and engineering.

KOJOSE also provides immediate open access to the journal content via TUBİTAK DergiPark system that makes research freely available to the public and supports a wider global exchange of knowledge. To provide greater visibility for researchers' work, the journal publishes original papers written in English. KOJOSE is also planning to publish special issues containing the best papers selected from various conferences in sub-fields of engineering, science and technology.

Finally, on behalf of the editorial team of KOJOSE, I would like to thank all the authors, readers, reviewers and editors, especially our associate editors Prof. Dr. **Murat HOŞÖZ** and Assoc. Prof. Dr. **Hikmet Hakan GÜREL** and our editorial team Asst. Prof. Dr. **Mihriban CİVAN**, Asst. Prof. Dr. **Recep Kaya GÖKTAŞ**, R.A. **Alp Eren ŞAHİN**, R.A. **Abdurrahman GÜN**, **Yusuf YAĞCI** (Instructor) and **Durmuş İMAT** (Executive Secretary) for their invaluable contribution to the journal development of high professional standards. I would also like to express my gratitude to the former director and associate directors of the Graduate School of Natural and Applied Sciences of Kocaeli University, in particular Prof. Dr. **Nilgün FIĞLALI**, Assoc. Prof. Dr. **Beyhan PEKEY**, and Assoc. Prof. Dr. **Recep Taygun GÜRAY**. Finally, I would like to thank Prof. Dr. **Sadettin HÜLAGÜ**, the Rector of Kocaeli University, for encouraging us to publish this journal.

May 2018  
Editor in Chief



**COVER PAGE** ..... **I**

**TABLE OF CONTENTS** ..... **II**

**REVISED** ..... **III**

**K. Süleyman YİĞİT**

Biogas Production from Dining Hall Waste and Landfill Leachate in a Two Stage R&D Facility 01-05  
(*Research Paper*)

**Z. Ezel DOĞAN, Fulya KAHRIMAN and Ş. Hakan ATAPEK**

Microstructural and Thermal Characterization of Aluminum Bronzes ..... 06-10  
(*Research Paper*)

**Hande BODUR, Sibel ÜNALDI , Sibel ÇİMEN and Gonca ÇAKIR**

A Novel Reflectarray Antenna with Reduced RCS..... 11-14  
(*Research Paper*)

**Sezgin BÜYÜKKÜTÜK and Günay ÖZTÜRK**

A Characterization of Factorable Surfaces in Euclidean 4-Space IE 4 ..... 15-20  
(*Research Paper*)



## Biogas Production from Dining Hall Waste and Landfill Leachate in a Two Stage R&D Facility

K.Süleyman YİĞİT<sup>1,\*</sup>,

<sup>1</sup> Department of Mechanical Engineering, Kocaeli University Graduate School of Natural and Applied Sciences, Kocaeli, 41380, Turkey

### Article Info

#### Research paper

Received : 22/02/2018

Accepted : 14/03/2018

#### Keywords

Anaerobic process  
Two stage biogas  
Dining hall waste  
Landfill leachate

### Abstract

Taking into consideration recovery of dining hall waste from university cafeteria and nutrient reduction of landfill leachate, they were mixed at a temperature of  $36\pm 1^\circ\text{C}$  and for a period of 90 days in a two stage biogas production R&D facility with a total volume of  $5\text{m}^3$ , and then experiments were done. Experiment-I was performed to engage the second digester as a priority, and Experiment-II was performed to engage the first digester. After the required bacteria formation was ensured, the first digester was daily fed with mixture of dining hall waste with 10% solid matter content and landfill leachate weighing 167 kg in total regularly feeding in Experiment-III. Analyses and measurements of total solids (TS), total volatile solids (TVS), C% and N% percentages, pH, volatile fatty acid (VFA) and inhibitive of the organic waste samples were measured from the feedstock, digesters, and fertilizer tanks. In addition, daily biogas samples were taken and concentrations of  $\text{CH}_4(\%)$  with mass flow rate of the biogas were measured. The results showed that in case dining hall waste and landfill leachate was mixed, the first digester worked at pH values of around 4.5–5.5 and performed the task of hydrolysis and acidification. The second digester performed the task of bio-methanation successfully.

## 1. Introduction

In developed countries, there has been an increased interest in the improvement of technologies for harnessing renewable energy sources such as biomass either directly or through conversion routes [1]. Valorization of biomass with electricity production or, even better, with cogeneration of heat and electricity are major contributing approaches to sustainable development [2]. Millions of tons of industrial, agricultural and domestic organic waste are attempted to be decomposed by burying systematically or nonsystematically, transformed into fertilizer by composting or disposed of by burning every year around the world. Organic waste buried non-systematically causes soil and water pollution to a large extent. At the same time, the emerging gas products cause air pollution and global warming [3–5]. During the decomposition of one ton organic solid matter, about  $50\text{--}110\text{ m}^3$  carbon dioxide ( $\text{CO}_2$ ) and  $90\text{--}140\text{ m}^3$  methane ( $\text{CH}_4$ ), are released into the atmosphere [6].  $\text{CH}_4$  has thirty times more effective on

global warming at a molecular scale compared to  $\text{CO}_2$  and its half-life is longer than other gases [3]. Anaerobic digestion process is applied to dispose of this type of organic waste without harming the environment [7]. Anaerobic digestion is a process where complex organic materials are transformed into volatile fatty acids by acid bacteria after the hydrolysis stage, and later to methane gas by methanogen bacteria. Methane fermentation is a complex process, which can be divided up into four phases: hydrolysis, acidogenesis, acetogenesis/dehydrogenation, and methanation. Hydrolytic bacteria bring about initial degradation of complex biopolymers such as cellulose, hemicelluloses, proteins and lipids into dicarboxylic acids, volatile fatty acids (VFAs), ammonia, carbon dioxide, and hydrogen. Methanogenic bacteria which play a key role in the terminal step of anaerobic digestion use only a few compounds like acetate, methanol, methylamine, hydrogen and carbon dioxide [8]. Successful applications of anaerobic technology depend on anaerobic digesters to a large extent [9–11]. In recent years, a series of new digester designs

\* Corresponding Author: kyigit@kocaeli.edu.tr

continue to be developed and an effort is made to advance from single-stage digesters to two-stage digesters [12]. In two stage biogas production facilities, it is possible to obtain high amounts of stable gas even in high loading ratios and realize production in higher efficiencies compared to that in single stage systems stated in their experimental studies that two stage systems are advantageous compared to single stage systems for domestic waste [13]. For these important reasons, it is foreseen that two stage biogas production systems will become widespread in industrial facilities soon [14]. For two stage systems to be preferable, more experimental studies must be performed, the ease of operation must be ensured and the investment costs must be lowered. Considering these facts, a two stage biogas production R&D facility able to work at actual conditions was designed, produced and installed by Kocaeli University together with the biogas working group of İzaydaş, 100% Kocaeli Metropolitan Municipality participation. This facility has been developed continually, and biogas production test studies have been conducted with various organic waste. In the studies performed, considering that methane formation process was very slow compared to fast formation of especially volatile fatty acids, the volumes of first digester 1.2 m<sup>3</sup> for hydrolysis and acidogen section, and second digester 3.8 m<sup>3</sup> for methanogen section were foreseen. The total system volume was maximum 5 m<sup>3</sup>; when needed, digesters can be operated under the specified volumes, and most suitable operational volumes and hydraulic retention times of both digesters, contents of the used organic material can be determined and adjusted according to operation analyses.

## 2. Working Method of the Two Stage Biogas Production R&D Facility

The schematic drawing of R&D-purpose two stage biogas production facility consisting of 1.2 m<sup>3</sup> first digester (for hydrolysis and acidification process) and 3.8 m<sup>3</sup> second digester (for the methanation process) is shown in Fig. 1. Disintegrator (1), feed mixer (2), stone, metal, glass retentive filter (4), first digester (3), second digester (5) and organic fertilizer storage tank (7) are connected serially to each other. (8: Gas pipeline, 9: Filter, 10: Gas engine and generator, 11: Main pipelines, 12: Electric control panel)

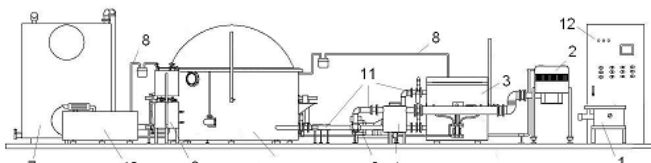


**Figure 1.** The schematic top view of biogas R&D facility.

The organic materials broken into small parts in the disintegrator were loaded into the feed mixer unit. Water requirement of the organic material loaded into the feed mixer was determined based on analyses and water or wastewater is automatically added into the feed mixing unit in the needed amount, and mixing is performed for certain duration. The product prepared in the feed mixer to be sent into the first digester is passed from the stone, metal, glass retentive filter, and the related pipes and valves on them are opened by the automation system for certain duration to ensure the daily feeding amount, the transfer pump is operated, and the product is transferred to the first digester. After completed the hydrolysis and acidification phases in the first digester, the product is transferred from the first digester to the second digester by means of the transfer pump by opening the related valves in the same amount again. The mixture is used by methane bacteria in the second digester for a longer retention duration and sent to the organic fertilizer storage tank by means of the related valves and transfer pump, and the biogas production process is completed. During the operation, the speed of mechanical mixing of digesters were set by the automation system. Heating system of both digesters operates with hot water passed inside heating pipes embedded within the concrete wall. In the case of any failure occurs in the heating system, concrete serves as thermal accumulator, and the energy stored within the concrete makes for energy losses of the system until the failure is rectified. Biogas is produced continuously within the first and second digester, and the biogas line is connected serially. Biogas coming from the first digester to the second digester combines with the gas produced in the second digester and sent into the gas cleaning unit. In this section, the H<sub>2</sub>S, other toxic constituents and water vapor in the biogas are retained and cleaned. For power generation, biogas is sent into the internal combustion engine and thus the engine and generator are operated. With the cooling water of the water-cooled gas engine, temperature of the digesters is kept fixed by means of the automation system.

## 3. Experimental Study and Results

The experimental study was conducted by using the continuous feed method. Experiments were lasted with the organic materials which can be seen in Table I for 90 days. The first two phases were aimed at engaging, while daily feedings were performed with various mixtures in the subsequent three phases. Due to experimental studies conducted successively, a two stage R&D purpose experiment system was used. Second digester engaging phase took 35 days, and first digester engaging phase operated during 16 days. In subsequent phases, hydraulic

retention period of the first digester took 6 days, and that of the second digester took 19 days, and experiments were conducted with different materials and mixture ratios at three separate phases. In experiment III, mixture of dining hall waste and landfill leachate were fed during 29 days. In the two stage R&D facility, in all phases of the experimental study, both digesters were operated at a mesophyllic temperature of  $37 \pm 0.1$  °C. Solid matter percentage of organic waste and landfill leachate were measured by drying with the humidity device at 105 °C, and that of volatile organic materials were measured by burning at 550 °C until the solid matter reaches fixed weighing for three hours, from the resulting amount of missing matter. Volatile fatty acids, total kjedhal nitrogen (TKN), ammonium, phosphate, sulphate, sulfide, nitrate and nitrite were analyzed with the Hach-Lange DR 5000 UV/VIS spectrophotometer, and metal and other trace elements with the 7500 CX, ICP-MS device. Samples were taken every day both in the first fed product and the first and second digesters, and once a week from the organic fertilizer storage tank and the total volatile fatty acid amount in the daily period, and variations of inhibitors and trace elements in the weekly period were tracked. Moreover, the amount of biogas produced was measured with biogas flowmeters, daily gas concentration [CH<sub>4</sub>(%), CO<sub>2</sub>(%), O<sub>2</sub>(%), N<sub>2</sub>(%), CO(ppm), H<sub>2</sub>S(ppm) and LEL(%)] with portable gas data LMS XI multifunction gas analyzer.

### 3.1. pH Change in the First and Second Digester

pH level of feeding products prepared in amounts 200 kg (mixture of 99 kg dining hall waste and 101 kg leachate), both digesters were measured regularly every day, and the obtained results are given in Fig 2.

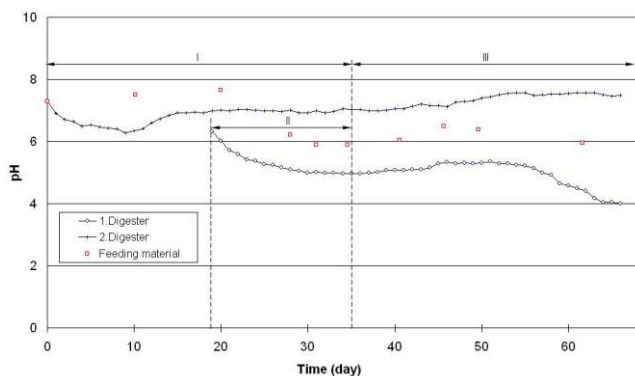


**Figure 2.** pH change in the feed material and the materials within the first and second digesters.

The pH in the second digester engaged initially with cow, chicken fertilizer, tripe interior, landfill leachate mixture were measured as 7.3 on the first day. This value

dropped rapidly to as low as 6.3 at the end of the 9 days, and afterwards, with the increase in methanogen bacteria, started to increase after day 11. In the first digester engaged on day 19, similar to the second digester, first digester pH value dropped rapidly in the beginning; on day 39, in order to slow this drop, feedback was done from the second digester with a pH value of 7 to the first digester. After day 35, when the pH decrease process of the first digester ended and the pH value became stable, 200 kg organic material was loaded regularly every day with dining hall waste and landfill leachate mixture. Beginning from day 35, when daily feedings began, it was observed that pH value of the material within the two digesters. In the engaging phase, average pH was around 5.2 in the 1<sup>st</sup> digester and 7 in the 2<sup>nd</sup> digester, respectively. As a result of experiments, it was seen that acidogen bacteria within the first digester in which the hydrolysis and acidogen process occurred produced volatile fatty acid at a pH of about 4– 5.

### 3.2. Volatile Fatty Acid (VFA) Concentration

Volatile fatty acids in the product within the first and second digesters were measured continuously during 65 days and obtained results are given in Fig. 3.

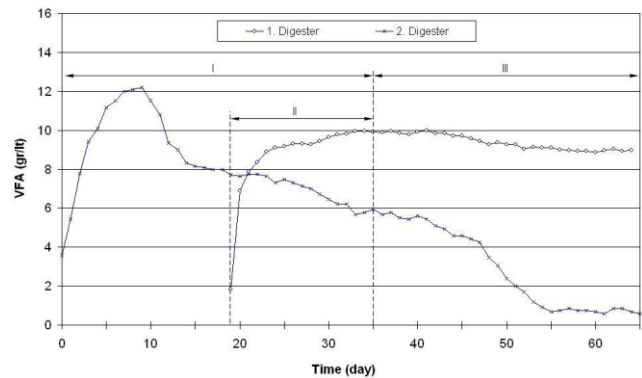


**Figure 3.** Volatile fatty acid change of the first and second digesters.

As explained above, volatile fatty acid of the product loaded into the second digester engaged first was initially measured as 3.5 g/l. In the first days when the experiment began, acidogen bacteria multiplied and volatile fatty acid value increased within the second digester. In the graphic given in Fig.3, volatile fatty acid amount of the second digester was maximum at 12 g/l on day 9. As numbers and activity of methanogen bacteria increased, so did their acetic acid consumption, and thus the volatile fatty acid value started to decrease. On day 19, initial loading of the mixture given in Table I into the first digester was done gradually. Because of the tripe interior material in the loading menu, it was observed that while pH dropped within the first digester, volatile fatty acid value increased rapidly.

Depending on the properties of dining hall waste and landfill leachate fed as part of the third experiment, it was seen that volatile fatty acids dropped from 10 to 9 g/l slowly in the first digester, and dropped from 6 to 0.5 g/l rapidly in the second digester. In summary, the first digester served as acidifier, and the second digester served as methanizer.

### 3.3. Methane Production in the First and Second Digesters

In the first digester engaged 19 days after the beginning of experimental study, as a result of the acidogen activity, high rates of CO<sub>2</sub> and volatile fatty acid formation, and low rates of methane formation occurred.

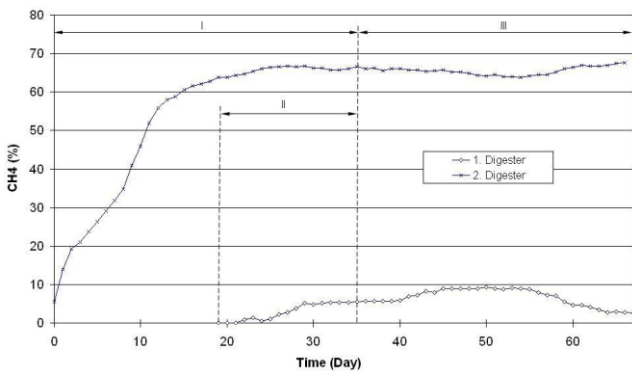


**Figure 4.** Methane percentage of biogas produced of first and second digesters.

It can be seen in Fig. 4 that on day 45 of the experiment the methane gas in the first digester reached its maximum value of 9 percent. Owing to the activity of acidogen bacteria in the first digester and unsuitability of pH value of the environment for methanogen bacteria, methane bacteria could not be engaged in sufficient activity, and in the subsequent periods of the future, methane was produced at an average level of 2%. The first digester worked for hydrolysis and acidification. In the second digester, naturally, as a result of acidogen activity at the beginning of experiments, high ratios of CO<sub>2</sub> formation was observed, methane gas started to increase rapidly on 8<sup>th</sup> day, CH<sub>4</sub>/CO<sub>2</sub> ratio surpassed 50% on day 12 and reached 68% on day 26. The experiment phase in III, feeding was performed daily from day 35 to day 65 with the loading menu consisting of dining hall waste and garbage seepage water. Methane content of the 29-day biogas production process is 65% on average.

### 3.4. Daily and Total Biogas Amount Produced in the First and Second Digesters

Daily biogas (methane) production of the first digester seen in Fig. 5 was 0.9 m<sup>3</sup>/day (3% CH<sub>4</sub>) on average between day 19 and day 35, 2.6 m<sup>3</sup>/day (8% CH<sub>4</sub>) on average between day 35 and day 65, and 0.9 m<sup>3</sup>/day (3% CH<sub>4</sub>) in the experiment.

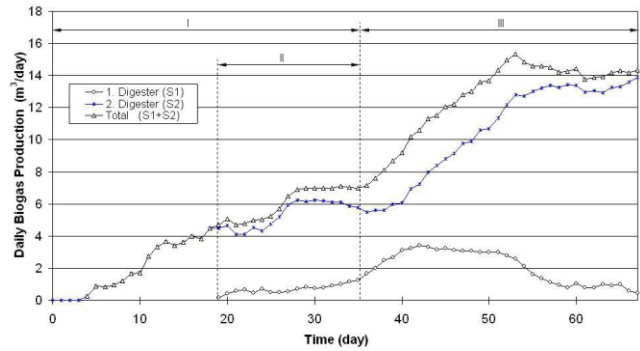


**Figure 5.** Daily biogas production of the first and second digesters.

Biogas production was 4 m<sup>3</sup>/day (51% CH<sub>4</sub>) on average from day of engaging the second to day 35; 13 m<sup>3</sup>/day (66% CH<sub>4</sub>) on average, from 36<sup>th</sup> day, when daily feeding with dining hall waste and landfill leachate mixture started.

Biogas amounts produced in both digesters were measured separately for 65 days and obtained results are given in Fig. 6. Accordingly, at the end of 65 days, 75 m<sup>3</sup> in the first digester, 389 m<sup>3</sup> in the second digester, and a total of 464 m<sup>3</sup> was produced from the two stage biogas system.

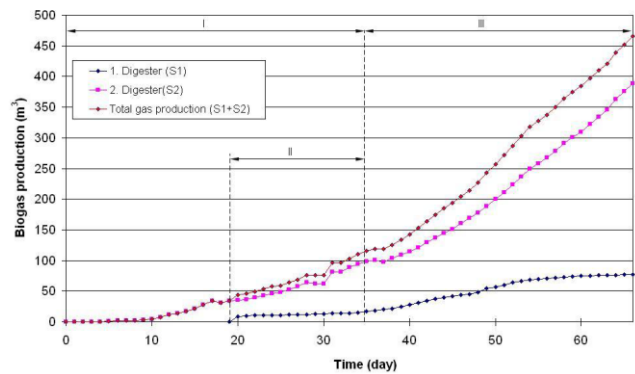


**Figure 6.** Total biogas production of the first and second digesters.

### 4. Conclusions

Storage of organic waste is a costly method with its environmental impacts. Biogas production with anaerobic digestion, one of the applicable methods for recovery, has been very important since biogas has a status of renewable

energy resource and ensures recycling. Obtaining the landfill leachate that may be needed for using organic waste by decomposing in anaerobic digester from regular storage areas continuing to form landfill leachate will lower purification costs. To this end, various organic materials with non-homogenous feeding conditions, such as dining hall waste, and landfill leachate were mixed and experiments were conducted in the two stage R&D experiment system. As a result of the experiments, it is highly possible to produce biogas by mixing various organic products and landfill leachate in two stage systems. In this process, the first digester served as acidifier, and second digester served as methanizer successfully.

### Acknowledgements

For our two stage study with organic waste and landfill leachate mixtures, I would like to extend our thanks to Izaydas General Manager Mr. Muhammet Sarac, Technical Services Manager Mr. Salih Deveci, former chief of maintenance workshop Mustafa Gunduz, Instrument maintenance chief Gulay Serit, especially Izaydas laboratory employee friends who made chemical analyses meticulously, technicians of Mechanic, Electrical and Instrument maintenance workshops who participated in the design, production, installation and trial works of the Biogas production R&D facility.

### References

- [1] Sivakumar P., Bhagiyalakshmi M., Anbarasu K., 2012. Anaerobic treatment of spoiled milk from milk processing industry for energy recovery – A laboratory to pilot scale study, *Fuel*, **96**(1), 482–486. DOI:10.1016/j.fuel.2012.01.046
- [2] Roubaud A., Favrat D., 2005. Improving performances of a lean burn cogeneration biogas engine equipped with combustion prechambers, *Fuel*, **84**(16), 2001–2007. DOI:10.1016/j.fuel.2004.02.023
- [3] Vieitez E.R., Grash S., 1999. Biogasification of solid waste by two-phase anaerobic fermentation, *Biomass and Bioenergy*, **16**(5), 299–309. DOI:10.1016/S0961-9534(99)00002-1
- [4] Kolbitsch P., Pfeifer C., Hofbauer H., 2008. Catalytic steam reforming of model biogas, *Fuel*, **87**(6), 701–706. DOI: 10.1016/j.fuel.2007.06.002
- [5] Effendi A., Hellgardt K., Zhang Z.G., Yoshida T., 2005. Optimising H<sub>2</sub> production from model biogas via combined steam reforming and CO shift reactions, *Fuel*, **84**(7-8), 869–874. DOI:10.1016/j.fuel.2004.12. 011
- [6] Macias-Corral M., Samani Z., Hanson A., Smith G., Funk P., Yu H., Longworth J., 2008. Anaerobic digestion of municipal solid waste and agricultural waste and the effect of co-digestion with dairy cow manure, *Bioresource Technology*, **99**(17), 8288–8293. DOI: 10.1016/j.biortech.2008.03.057
- [7] Park W.J., Shin C.H., 2001. Surface emissions of landfill gas from solid waste landfill, *Atmospheric Environment*, **35**(20), 3445–3451. DOI: 10.1016/S1352-2310(01)00118-2
- [8] Gupta P., Singh R.S., Sachan A., Vidyarthi A.S., Gupta A., 2012. Study on biogas production by anaerobic digestion of garden-waste, *Fuel*, **95**, 495–498. DOI: 10.1016/j.fuel.2011.11.006
- [9] Bouallagui H., Torrijos M., Godon J.J., Moletta R., Cheikh R.B., Touhami Y., Delgenes J.P., Hamdi M., 2004. Two-phases anaerobic digestion of fruit and vegetable wastes: Bioreactors performance, *Biochemical Engineering Journal*, **21**(2), 193–197. DOI: 10.1016/j.bej.2004.05.001
- [10] Brummeler E.T, Aarnink M.J., Koster I.W., 1992. Dry anaerobic digestion of solid organic waste in a biocell reactor at a pilot-plant scale, *Water Science Tech.*; **25**(7), 301–10
- [11] Ghosh S., 1995. Role of anaerobic digestion in alleviating environmental problems in The United States, *Coast and Environmental Engineering*, **1995**(521), 239–248. DOI: 10.2208/jscej.1995. 521\_239
- [12] Liu G, Zhang R, Li X, Dong R., 2007. Research progress in anaerobic digestion of high moisture organic solid waste, *Agricultural Engineering International: the CIGR E Journal*, **9**(13)
- [13] Bhattacharyya J.K., Kumar S., Devotta S., 2008. Studies on acidification in two-phase biomethanation process of municipal solid waste, *Waste Management*, **28**(1), 164–69. DOI: 10.1016/j.wasman.2006.11.014
- [14] Parawira W., Murto M., Read JS, Mattiasson B., 2005. Profile of hydrolases and biogas production during two-stage mesophilic anaerobic digestion of solid potato waste, *Process Biochemistry*, **40**(9), 2945–2952. DOI: 10.1016/j.procbio.2005.01.010



## Microstructural and Thermal Characterization of Aluminum Bronzes

Z.Ezel DOĞAN<sup>1</sup>, Fulya KAHRIMAN<sup>1</sup>, Ş. Hakan ATAPEK<sup>1,\*</sup>

<sup>1</sup>Metallurgical and Materials Engineering, Kocaeli University, Kocaeli, 41380, Turkey

### Article Info

#### Research paper

Received : 14/03/2018

Accepted : 15/05/2018

### Keywords

Aluminum bronze  
Solidification  
Microstructure  
Characterization

### Abstract

In this study, microstructures and the solidification characteristics of heat treatable Cu-Al-Fe-Ni based alloys were investigated. Initial microstructural features of conventional alloys were examined by microscopical analysis and not only the martensitic structure but also several kappa phases embedded in copper based matrix were observed. Then, thermal analysis was performed in order to reveal the solidification sequence under cooling and the findings on the crystallization were in good agreement with the data reported earlier.

## 1. Introduction

Aluminum bronzes, especially nickel-aluminum ones, are widely used in chemical plants, marine parts, aviation and bearing systems due to their high strength, corrosion and wear resistance. These alloys are heat treatable alloys and contain 8-14 % Al, 2-4 % Mn, Ni and Fe. Their microstructural features vary as a function of both casting process and heat treatment procedures. By casting, a typical nickel-aluminum bronze solidifies at the temperature around 1070 °C and the alloy has a great diversity of microstructural features during slow cooling to room temperature. By heat treatment procedure consisting of solution annealing, quenching and tempering, a tempered martensitic/bainitic microstructure could be achieved and these structures enhance the mechanical properties of the nickel-aluminum bronzes [1-5].

According to Cu-Al equilibrium diagram [6], the structure of aluminum bronze consists of  $\alpha$ -phase,  $\beta$ -phase,  $\gamma$ -phase and several electronic compounds (Cu<sub>3</sub>Al, Cu<sub>32</sub>Al<sub>19</sub> etc.), however, many alloying elements (Fe, Mn and Ni) are responsible for the formation of several precipitates known as kappa phases. The mechanical properties are also affected by these precipitates [7-10].

The type and amount of these precipitates could be changed as a function of the applied heat treatment routes. In the re-design of the bronze matrix, both solution annealing and tempering temperature play an important role and all exothermic/endothermic reactions related to the phase transformation can be investigated.

In this study, two commercial nickel-aluminum bronzes having different iron and manganese content were provided and their both microstructural features and solidification characteristics were characterized by metallurgical and thermal analysis. The results showed that the amount of iron and manganese are very effective on the type and amount of kappa precipitates and also on the solidification path of the studied alloys.

## 2. Materials and Methods

Cast and forged Cu-9Al-3Fe-5Ni-1Mn and Cu-10Al-4.8Fe-5Ni-1.5Mn alloys were provided from Sağlam Metal Co. The characterization studies were carried out in two stages; (i) microstructural characterization and (ii) thermal analysis. In microstructural characterization, samples were prepared by metallographically. The samples were ground with 320, 600, and 1000 mesh size SiC

\* Corresponding Author: [hatapek@kocaeli.edu.tr](mailto:hatapek@kocaeli.edu.tr)

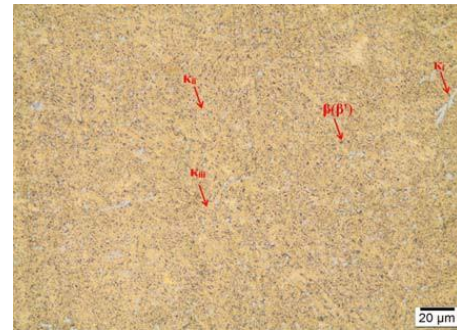
abrasives, and then polished with 3  $\mu\text{m}$  diamond solution. Polished surface was etched by a solution including 50 ml HCl, 10 ml  $\text{HNO}_3$ , 10 g FeCl, 100 ml  $\text{H}_2\text{O}$ . Microstructural characterization was carried out using light microscope (LM, Olympus BX41M-LED) and scanning electron microscope (SEM, Jeol JSM 6060). In order to determine solidification characteristics of the studied alloys, thermal analysis was conducted. The thermal analysis were carried out by using differential thermal analysis (DTA) and differential scanning calorimeter (DSC) method on Netzsch STA 409 PG Luxx. The samples were heated to 1100  $^\circ\text{C}$  with a heating rate of 5  $\text{K}\cdot\text{min}^{-1}$ , held at that temperature for 5 min, and then cooled to room temperature (RT) with a rate of 5  $\text{K}\cdot\text{min}^{-1}$ .

### 3. Results and Discussion

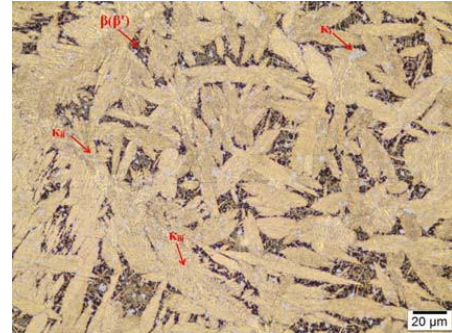
#### 3.1. Microstructural characterization

As reported in previous studies for a solidified nickel-aluminum bronze [11, 12], the microstructure consists entirely of  $\beta$ -phase until the alloy is cooled down below 1030  $^\circ\text{C}$  and  $\alpha$ -phase forms within  $\beta$ -phase. About 930  $^\circ\text{C}$ , a globular intermetallic phase ( $\kappa_{ii}$ ) begins to form within  $\beta$ -phase and a coarser intermetallic phase ( $\kappa_i$ ) is appears within the  $\beta$ -phase due to higher iron content. When the temperature falls down to 860  $^\circ\text{C}$ , another intermetallic phase ( $\kappa_{iv}$ ) starts to form within  $\alpha$ -phase as a function of iron content. At 800  $^\circ\text{C}$ , due to the eutectoid reaction, the remaining  $\beta$ -phase is transformed to the intermetallic  $\kappa_{iv}$  phase. In fact, it is expected that the solidified structure consists of several kappa phases embedded in  $\alpha$ -phase, however, if the cooling rate is higher, some  $\beta$ -phase remains and the matrix includes  $\beta'$ -phase known as retained  $\beta$ -phase.

Figure 1 shows the microstructures of studied alloys and all microstructural features within alloy matrices are introduced. Generally the microstructure consists of grains of  $\alpha$  phase (fcc copper-rich solid solution), a small volume fraction of  $\beta(\beta')$  phase (solid solution with martensitic structure) and intermetallic  $\kappa$  phases. The  $\kappa_i$  phases appears as the rosette-like precipitates and these precipitates are based on  $\text{Fe}_3\text{Al}$ . The dendritic-shaped precipitates are  $\kappa_{ii}$  phases; they are not only distributed at the  $\alpha/\beta$  boundaries but also smaller than  $\kappa_i$ . The matrices have lamellar or globular eutectoidal decomposition products known as Ni-rich (NiAl)  $\kappa_{iii}$  phases. The Fe-rich  $\kappa_{iv}$  phases are very fine particles and they are visible within the high resolution SEM image given in Figure 2. The elemental distribution was also studied and the micrographs given in Figure 3 shows the Al, Fe and Ni-rich kappa phases embedded in copper based matrix.

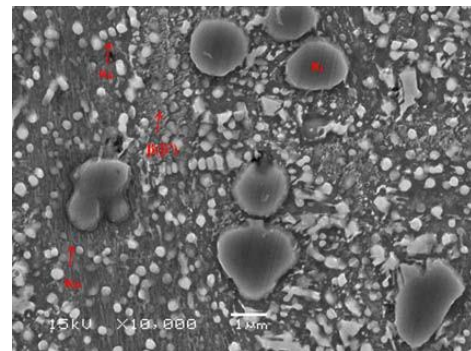


(a)

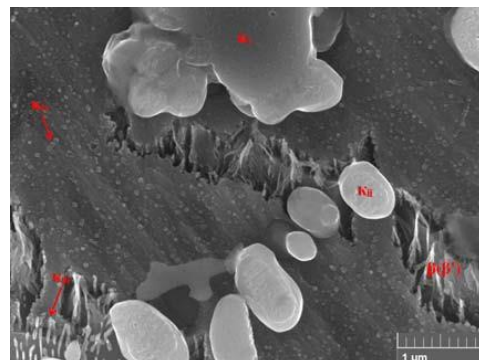


(b)

**Figure 1.** LM images showing the matrices of studied alloys; (a) Cu-9Al-3Fe-5Ni-1Mn and (b) Cu-10Al-4.8Fe-5Ni-1.5Mn.



(a)



(b)

**Figure 2.** SEM images showing the obtained phases Cu-9Al-3Fe-5Ni-1Mn (a) and Cu-10Al-4.8Fe-5Ni-1.5Mn (b).

### 3.2. Thermal characterization

The solidification sequences of each alloy were determined by both DTA and DSC analysis and the obtained thermograms are given in Figure 3. In thermograms, several phase transformations were observed. In the Cu-Al-Fe-Ni system the following six reactions could be observed by TDA (Thermal Derivative Analysis) and these reactions include not only liquid-solid/solid-solid phase transformations but also precipitation reactions; (i)  $\beta$  crystallization from liquid, (ii) both  $\kappa_i$  and  $\kappa_{ii}$  precipitation within  $\beta$ -phase, (iii)  $\alpha$  crystallization from  $\beta$ -phase, (iv)  $\kappa_{iii}$  precipitation within  $\alpha$ -phase, (v)  $\kappa_{iv}$  precipitation within  $\alpha$ -phase and (vi) eutectoid transformation ( $\beta \rightarrow \alpha + \gamma_2$ ) [13]. However, no exothermic data on the precipitation of  $\kappa$  phases was determined in both DTA and DSC analysis.

In the Cu-Al-Fe-Ni system,  $\beta$ -phase was crystallized from liquid and both liquidus and solidus temperature was affected by the alloying elements, especially Al, Fe etc. The data obtained from thermal analyzes showed that the alloy having higher Al, Fe and Mn (Cu-10Al-4.8Fe-5Ni-1.5Mn) had an expanded solidification range, since the curves shifted to higher liquidus and solidus temperatures. The thermograms have no information on the crystallization of  $\kappa_i$  and  $\kappa_{ii}$  precipitation. Brezina [14] had studied on the crystallization of Cu-10Al-5Fe-5Ni and did not also explain clearly the stage of formation of  $\kappa_i$  phases. These phases preferably form in the grain boundaries of  $\beta$ -phase and the possibility of crystallization is affected by the portion of iron-rich liquid. Although no data on the exothermic reaction for  $\kappa_{ii}$  precipitation was obtained, Pisarek studied on the model of Cu-Al-Fe-Ni bronze crystallization and reported that  $\kappa_{ii}$  precipitates within  $\beta$ -phase at 897 °C [13]. In the studied system, there is a well-known solid-solid reaction and  $\alpha$ -phase forms from  $\beta$ -phase. According to the thermograms given in Figure 4,  $\alpha$ -phase crystallization in the alloy having higher Al, Fe and Mn content (Cu-10Al-4.8Fe-5Ni-1.5Mn) started within the range of 810-812 °C and the obtained data were in good agreement with the reported data in Ref. 14, since DTA studies revealed that the temperature of  $\alpha$ -phase crystallization was 812 °C for Cu-Al-Fe-Ni system.

As mentioned before, the  $\kappa_{iii}$  precipitation could be accompanied with the formation of  $\alpha$ -phase and the crystallization range of 715-800 °C is attributed to

formation of  $\kappa_{iii}$  phase for the studied alloys. On the other hand, the thermograms also point out the eutectoid transformation and DTA analysis showed that this transformation started at 502 °C and 522 °C for Cu-9Al-3Fe-5Ni-1Mn and Cu-10Al-4.8Fe-5Ni-1.5Mn alloys, respectively. In DSC analysis, these temperatures were obtained as 500 °C and 513 °C for Cu-9Al-3Fe-5Ni-1Mn and Cu-10Al-4.8Fe-5Ni-1.5Mn alloys, respectively.

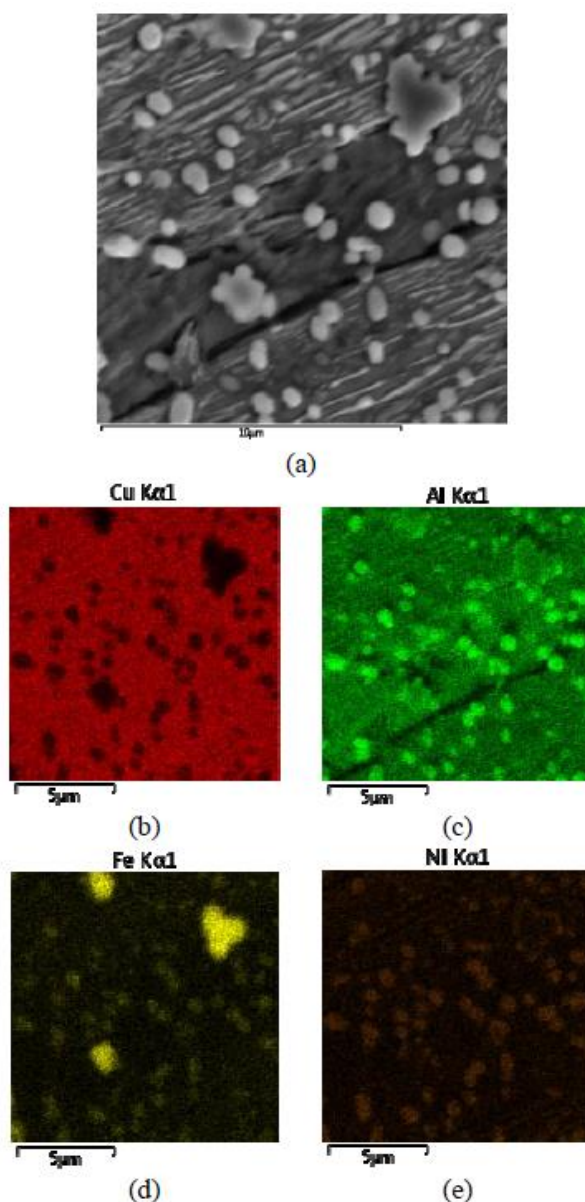


**Figure 3.** SEM images showing the elemental distribution of kappa phases embedded in  $\alpha$ -Cu matrix of Cu-10Al-4.8Fe-5Ni-1.5Mn (a), the distribution of Cu (b), Al (c), Fe (d) and Ni atoms (e)

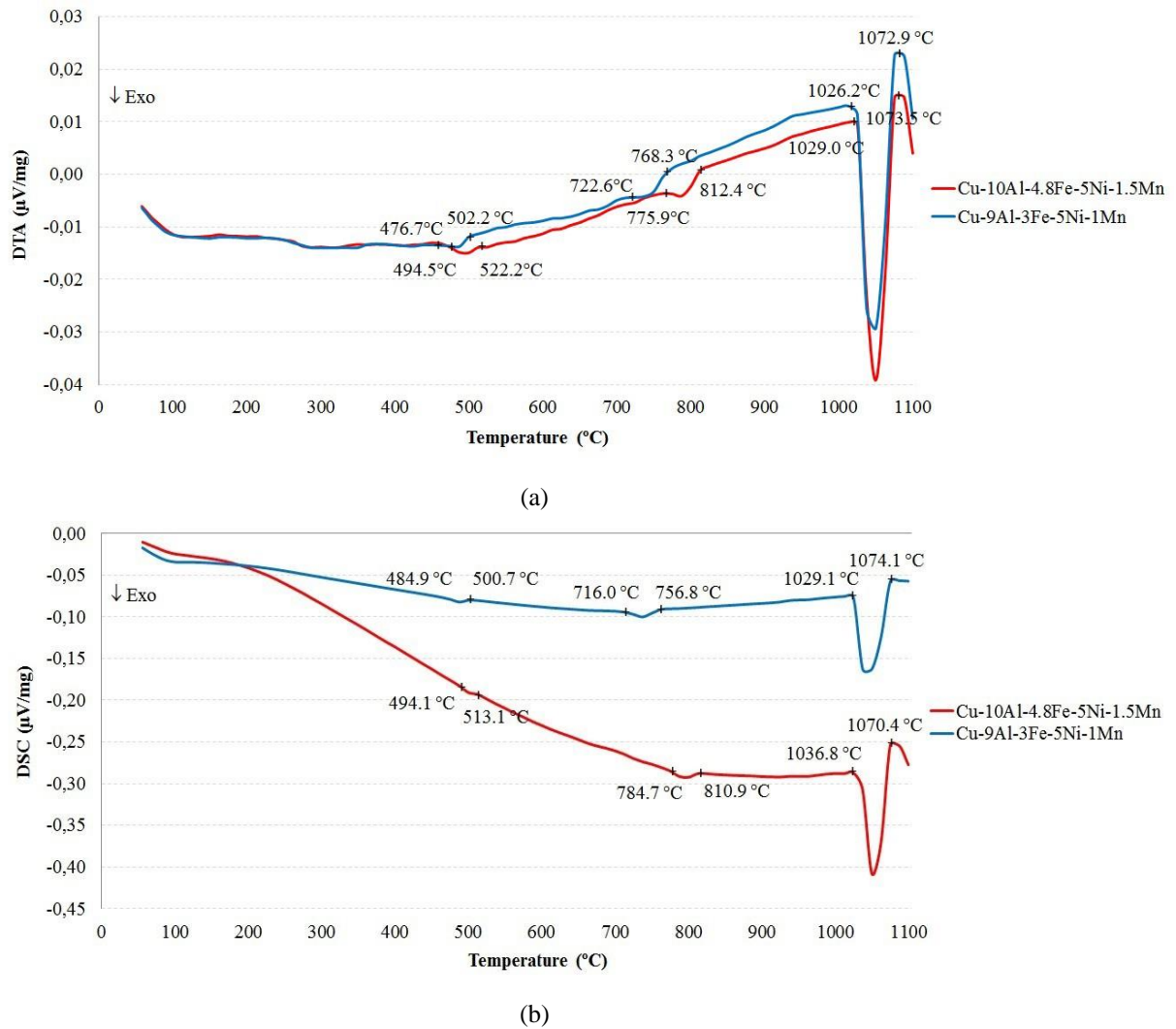


**Figure 4.** Thermograms showing the solidification sequence of the studied alloys; (a) DTA and (b) DSC.

#### 4. Conclusions

In this study, both microstructural and thermal characterizations of two conventional Al-bronzes were investigated and the following results were obtained;

(i) The alloys had similar microstructural features and their matrices consisted of  $\beta(\beta')$  and several kappa phases embedded in  $\alpha$ -Cu. Although no morphological changes on kappa phases were observed, the amounts of these phases were varied as a function of the chemical composition of the studied alloy.

(ii) The solidification sequences of the alloys were also studied and the obtained data was in good agreement with the ones reported earlier [13, 14] and higher Al, Fe and Mn content caused a shift on the curves, thus all liquid-solid/solid-solid reactions started at higher temperatures.

#### References

[1] Kaplan M., Yildiz A. K., 2003. The effects of

production methods on the microstructures and mechanical properties of an aluminum bronze. *Materials Letters* **57**, 4402-4411.

[2] Anantapong J., Uthaisangsuk V., Suranuntchai S., Manonukul A., 2014. Effect of hot working on microstructure evolution of as-cast nickel aluminum bronze alloy. *Materials and Design* **60**, 233-243.

[3] Wu Z., Cheng Y. F., Liu L., Lv W., Hu W., 2015. Effect of heat treatment on microstructure evolution and erosion-corrosion behavior of a nickel-aluminum bronze alloy in chloride solution. *Corrosion Science* **98**, 260-270.

[4] Li W. S., Wang Z. P., Lu Y., Jin Y. H., Yuan L. H., Wang F., 2006. Mechanical and tribological properties of a novel aluminum bronze material for drawing dies. *Wear* **261**, 155-163.

[5] Chen R. P., Linag Z. Q., Zhang W. W., Zhang D. T., Luo Z. Q., Li Y. Y., 2007. Effect of heat treatment on microstructure and properties of hot-extruded nickel-aluminum bronze. *Transactions of Nonferrous Metals*

Society of China **17**, 1254-1258.

[6] Copper Development Association, 1992. Equilibrium diagrams, selected copper alloy diagrams illustrating the major types of phase transformation, CDA Publication No 94.

[7] Al-Hashem A., Riad W., 2002. The role of microstructure of nickel-aluminium-bronze alloy on its cavitation corrosion behavior in natural seawater. *Materials Characterization* **48**, 37-41.

[8] Lv Y., Wang L., Han Y., Xu X., Lu W., 2015. Investigation of microstructure and mechanical properties of hot worked NiAl bronze alloy with different deformation degree. *Materials Science & Engineering A* **643**, 17-24.

[9] Xu X., Lv Y., Hu M., Xiong D., Zhang L., Wang L., Lu W., 2016. Influence of second phases on fatigue crack growth behavior of nickel aluminum bronze. *International Journal of Fatigue* **82**, 579-587.

[10] Fonlupt S., Bayle B., Delafosse D., Heuze J.L., 2005. Role of second phases in the stress corrosion cracking of a nickel-aluminum bronze in saline water. *Corrosion Science* **47**, 2792-2806.

[11] Feest E. A., Cook I. A., 2013. Pre-primary phase formation in solidification of nickel-aluminium bronze. *Journal of Metals Technology* **10**, 121-124.

[12] Cenoz I., 2010. Metallography of aluminium bronze alloy as cast in permanent iron die. *Association of Metallurgical Engineers of Serbia, AMES* **16**, 115-122.

[13] Pisarek B. P., 2013. Model of Cu-Al-Fe-Ni bronze crystallization. *Archives of Foundry Engineering* **13**, 72-79.

[14] Brezina P., 1973. Gefügeumwandlungen und mechanische eigenschaften der mehr- aluminiumbronzen vom typ CuAl10Fe5Ni5. *Giesserei-Forschung* **25**, 1-10.



## A Novel Reflectarray Antenna with Reduced RCS

Hande Bodur<sup>1,\*</sup>, Sibel Ünalı<sup>2</sup>, Sibel Çimen<sup>1</sup> and Gonca Çakır<sup>1</sup>

<sup>1</sup> Electronics and Communications Engineering, Kocaeli University, Kocaeli, 41380, Turkey

<sup>2</sup> Electrical and Electronics Engineering, Bilecik Şeyh Edebalı University, Bilecik, 11230, Turkey

### Article Info

#### Research paper

Received : 27/02/2018

Accepted : 31/03/2018

#### Keywords

Frequency selective surface  
Microstrip reflectarray antenna  
X-Band  
Radar cross section

### Abstract

A novel frequency selective surface (FSS) configuration in the reflectarray antenna is proposed for the reduction of radar cross section (RCS) level in this work. Double-layer FSS structure is located behind the reflectarray antenna as a ground. A 9×9 elements FSS with variable size patches has same geometry with the reflectarray antenna. The RCS reduction performance of reflectarray antenna for both ground plane backed and FSS backed is compared. The results of simulation are obtained by using CST Microwave Studio. The simulation results show that RCS level of FSS backed reflectarray antenna is reduced both in-band (8-12 GHz) and out-of-band (2-7 GHz and 13-18 GHz). In the literature, RCS reduction of reflectarray antenna with FSS structure has only been achieved out-of-band. Furthermore, the gain and radiation performance of the ground plane backed reflectarray antenna and FSS backed reflectarray antenna are compatible with each other.

## 1. Introduction

High gain antennas are used in communication systems and radar applications. In recent years, reflectarray antennas have commonly been preferred instead of the conventional parabolic reflectors when the high gain antennas are required [1]. It has several advantages such as which are low profile, low cost, light weight, no any feeding networks, easy fabrication and electronically beam direction [2-4].

It is well known that the use of high gain antennas increases the RCS level on military applications (aircraft, ships and so on) and the platform detectability [5]. The numbers of studies to reduce RCS in the reflectarray antennas are limited in the literature. Especially, RCS reduction of reflectarray antenna with FSS structure has only been achieved out-of-band.

General methods for reducing RCS included in the literature are radar absorbing material (RAM) coating [6], passive or active cancellations [7], antenna forming [8] and using FSS [9-11]. In particular, the studies on RCS reduction of microstrip reflectarray antennas with FSS structure are both very narrow and only out-of-band. In the following

works, RCS cannot be reduced in the operating band of reflectarray antenna [5], [11], [12]. In this study, it has been selected a new type FSS structure for the RCS reduction of reflectarray antenna. As compared with the previous works, current method can strongly reduce the RCS both in-band and out-of-band with same gain and radiation performance.

In this paper, 9×9 elements reflectarray antenna with double-layer FSS, which are located behind the reflectarray antenna, is designed and simulated. FSS structure has the same size and arrangement with the reflectarray antenna. We showed that RCS level of the reflectarray antenna has been reduced in-band and out-of-band when ground plane is replaced with FSS. The similar RCS reduction method with [13] is used in this study. But using different geometry of unit cell and FSS settlement, more RCS reduction is achieved in the operating band as compared to [13]. RCS level is reduced by 14.8 dB in-band at 9 GHz and by 17 dB out of the operation band at 5 GHz. Gain and radiation performance of the original reflectarray antenna is preserved and so the results are nearly similar between FSS backed and ground plane backed reflectarray antenna.

\* Corresponding Author: hande.bodur@kocaeli.edu.tr

## 2. Design Procedure of the Proposed Work

could help to extend the bandwidth.

### 2.1. Reflectarray Antenna Structure

In this study, a reflectarray antenna that is previously presented in reference [15] is used for reduction of RCS level. This reflectarray antenna has  $9 \times 9$  elements with the length of  $17 \times 17$  mm in  $xy$ -plane. The unit cell of the reflectarray is composed of double rings and it is shown in Fig. 1. Based on parametric study, the parameters of the unit cell are chosen as follow:  $R_1$  = variable (2 mm – 6.5 mm),  $R_2 = b \times R_1$ ,  $L_1 = a \times R_1$ ,  $L_2 = a \times R_2$ ,  $a = 1.4$ ,  $b = 0.6$ ,  $air = 5.5$  mm and length of unit cell  $D = 17$  mm. The substrate of unit cell is chosen Arlon AR 600 ( $\epsilon_r = 6.15$ ) with thickness  $h = 0.508$  mm. The air gap of between substrate and ground plane is 5.5 mm. The phase range of reflectarray antennas is desired generally more than  $360^\circ$  [14]. In this unit cell design,  $410^\circ$  phase range is obtained by varying of patches size at the center frequency  $f = 10$  GHz. Fig. 2 shows smooth and linear reflection phase curve at 10 GHz by varying of  $R_1$ , which

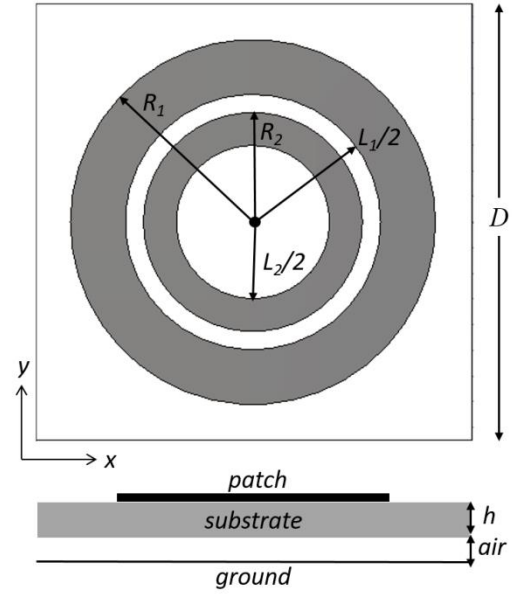


Figure 1. The view of reflectarray unit cell.

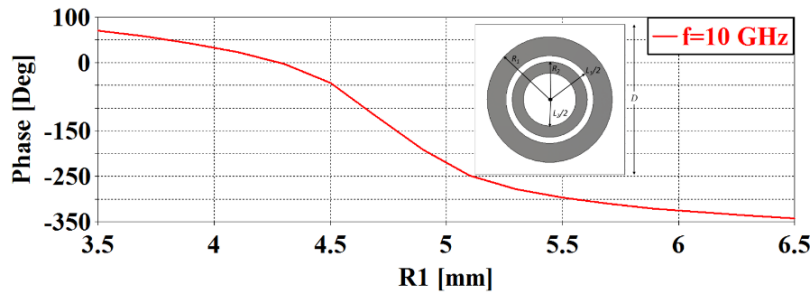


Figure 2. Reflection phase curve of the unit cell.

Table 2. The list of parameters.

$D = 17$ mm	$a = 1.4$
$R_1 =$ variable	$b = 0.6$
$R_2 = b \times R_1$	$\epsilon_r = 6.15$
$L_1 = a \times R_1$	$h = 0.508$ mm
$L_2 = a \times R_2$	$air = 5.5$ mm

### 2.2. FSS Backed Reflectarray Antenna

RCS reduction is achieved by using double-layer FSS which are located behind the reflectarray antenna. The identical reflectarray settlement is used as a FSS ground plane. Between reflectarray surface and each layer has 5.5 mm air gap as shown in Fig. 3. Double-layer arrangement behind the reflectarray is illuminated by pyramidal horn antenna (Fig. 4). The pyramidal horn antenna is a horn antenna with  $61 \text{ mm} \times 45 \text{ mm}$  aperture size and has 120 mm tapering length. It is located at  $F = 264$  mm focal distance

between array surface and horn aperture. Also simulated radiation patterns of horn antenna are given at 10 GHz for E-plane and H-plane (Fig. 5). As seen from the Fig. 5 the pyramidal horn antenna has 3-dB beam-width approximately  $30^\circ$ .

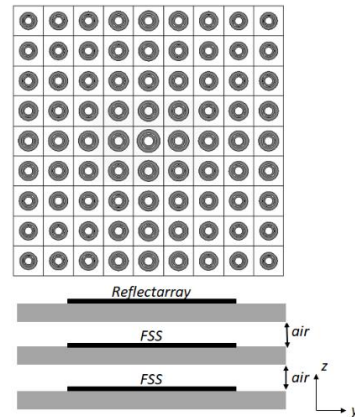


Figure 3. Reflectarray structure and double-layer settlement behind the reflectarray antenna used for FSS layer.

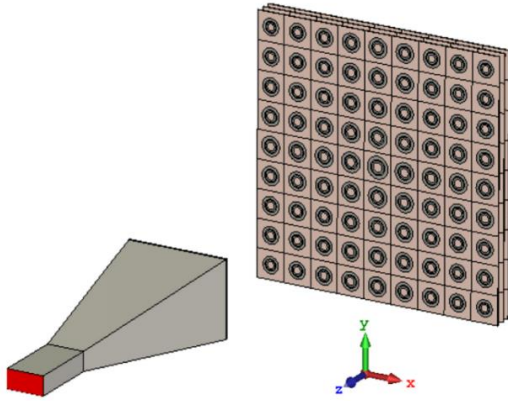


Figure 4. Reflectarray antenna with FSS backed.

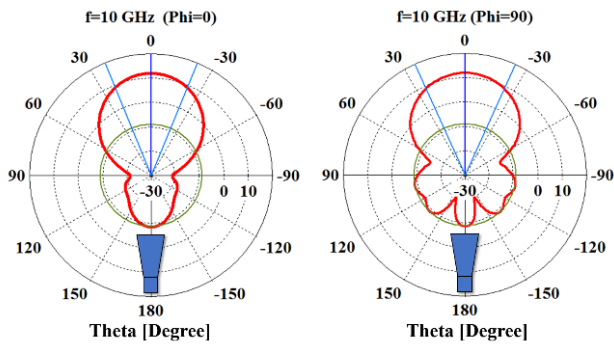


Figure 5. Simulated radiation patterns of horn antenna at 10 GHz for E-plane and H-plane.

### 3. Simulation Results

In order to reduce of RCS level, ground plane of reflectarray antenna is replaced with FSS. In Fig. 6, it is been demonstrated the comparison of the reflection coefficient of reflectarray antenna with ground plane backed and FSS backed. Reflection characteristics are not completely different from the each other in each case. Simulation results show the relationship between the monostatic RCS levels of the ground plane backed reflectarray antenna and FSS backed reflectarray antenna in Fig. 7. Double-layer FSS backed on the reflectarray reduced the RCS level in-band and out-of-band visibly. RCS reduction is obtained up to 14.8 dB in-band at 9 GHz and up to 17 dB out-of the operation band at 5 GHz.

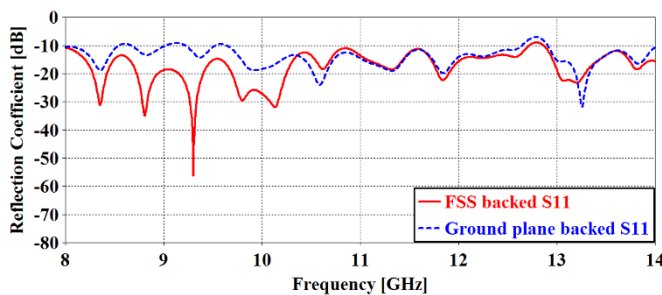


Figure 6. S<sub>11</sub> parameter of reflectarray antenna with ground plane backed and FSS backed.

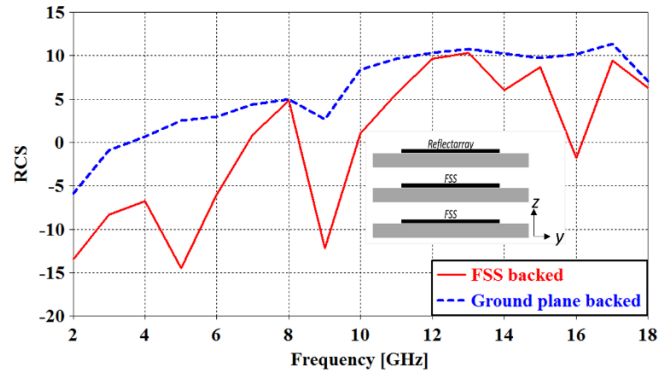


Figure 7. Relationship between the monostatic RCS levels of the ground plane backed and FSS backed reflectarray antennas.

Gain results between FSS backed and ground plane backed reflectarray antennas can be observed from Figure 8.

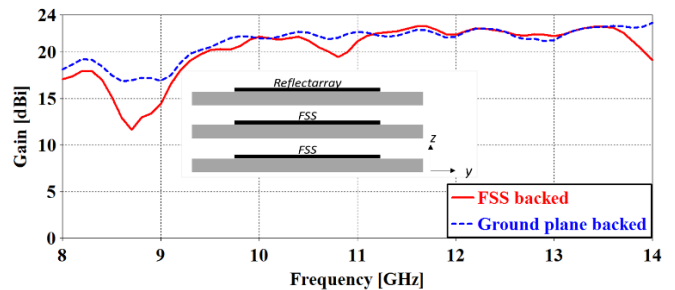
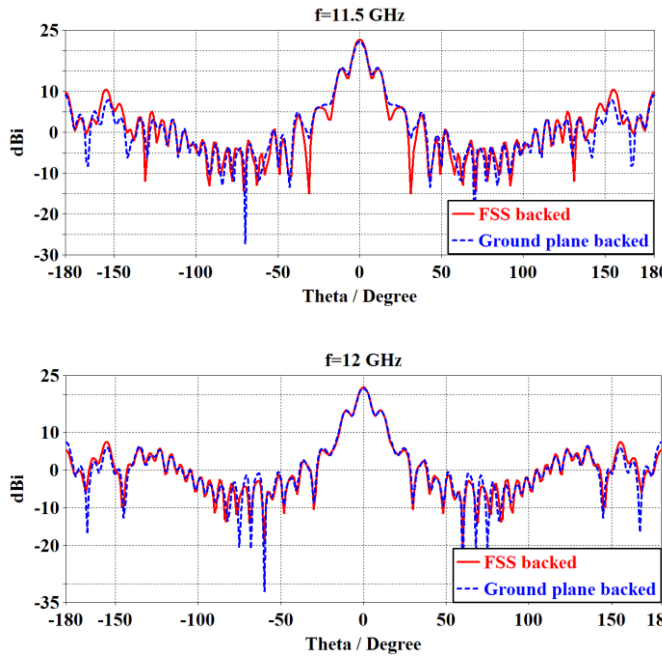


Figure 8. Gain curves for the ground plane backed reflectarray antenna and FSS backed reflectarray antenna.

A suitable FSS is integrated into the reflectarray antenna as a ground for lowering the RCS level without any changes of radiation performance. So the effects of the FSS backed reflectarray design are investigated on performance of the reflectarray. For this purpose, gain curve of ground plane backed and FSS backed are compared to each other. Fig. 8 shows that the gain curves of the reflectarray antennas in two cases are in a harmony with each other.

Fig. 9 shows the comparison of the radiation pattern of the FSS backed and ground plane backed reflectarray antenna at 11.5 GHz and 12 GHz respectively. As seen from the figures, directivity of the FSS backed and ground plane backed reflectarray antenna has been stable.



**Figure 9.** Radiation patterns of FSS backed and ground plane backed reflectarray antenna at 11.5 GHz and 12 GHz ( $\phi=90^\circ$ ).

#### 4. Conclusions

A novel double-layer FSS structure has been located behind the reflectarray antenna as a ground for RCS reduction. CST Microwave Studio is used for simulation of the traditional reflectarray with ground plane backed and new configuration of reflectarray. The simulation results show that the FSS-ground has reduced the RCS level in-band as well as out-of-band as compared to the only ground-plane backing, while the gain and radiation performance of the antenna is almost maintained the same for both configurations.

#### Acknowledgements

This work supported by of The Scientific and Technological Research Council of Turkey (TUBITAK) (Project No: 114E500).

#### References

[1] Huang J., Encinar J.A., 2008. Reflectarray Antennas, IEEE Press/Wiley, Piscataway, NJ, USA.

[2] Carrasco E., Barba M., Encinar J.A., Arrebola M., 2013. Design, manufacture and test of a low-cost shaped-beam reflectarray using a single layer of varying-sized printed dipoles. *IEEE Trans. On Antennas and Propagation* **61**, 3077-3085.

[3] Zubir F., Rahim M.K.A., Ayop O.B., Majid H.A., 2010. Design and analysis of microstrip reflectarray antenna with

Minkowski shape radiation element. *Progress In Electromagnetics Research Letters* **24**, 317-331.

[4] Tahir F.A., Aubert H., Girard E., 2010. Equivalent electrical circuit for designing MEMS-controlled reflectarray phase shifters. *Progress In Electromagnetics Research Letters* **100**, 1-12.

[5] Fakharian M.M., Rezaei P., Orouji A., 2014. A Reflectarray based on the folded SIR patch-slot configuration backed on FSS for low RCS. *Progress In Electromagnetics Research Letters* **47**, 119-124.

[6] Peixoto G.G., De Paula A.L., Andrade L.A., Lopes C.M.A., Rezende M.C., 2005. Radar absorbing material (RAM) and shaping on radar cross section reduction of dihedral comers. Paper presented at SBMO/IEEE MTT-S International Conference on Microwave and optoelectronics, Brasilia, Brazil, 25 July.

[7] Knott E.F., Shaeffer J.F., Tuley M.T., 2004. Radar Cross Section, Raleigh, SciTech, NC, USA.

[8] Jiang, W., Hong, T., Liu, Y., Gong, S. X., Guan, Y., Chui S., 2010. A novel technique for radar cross section reduction of printed antennas. *Journal of Electromagnetic Waves and Applications* **24**, 1-60.

[9] Genovesi S., Costa F., Monorchio A., 2012. Low-profile array with reduced radar cross section by using hybrid frequency selective surfaces. *IEEE Trans. Antennas Propag* **60**, 2327-2335.

[10] Misran N., Cahill R., Fusco V.F., 2003. RCS reduction technique for reflectarray antennas. *Electron. Letters* **39**, 1630-1631.

[11] Li H., Wang B.-Z., Zheng G., Shao W., Guo L., 2010. A reflectarray antenna backed on FSS for low RCS and high radiation performances. *Progress In Electromagnetics Research C* **15**, 145-155.

[12] Ren, L.-S., Jiao, Y.-C., Zhao, J.-J., Li, F., 2011. RCS reduction for a FSS-backed reflectarray using a ring element. *Progress In Electromagnetics Research Letters* **26**, 115-123.

[13] Bodur H., Ünalı S., Çimen S., Çakır G., 2017. A novel reflectarray antenna backed with double layer FSS for RCS reduction. Paper presented at International Applied Computational Electromagnetics Society (ACES) Symposium, Florence, Italy, 26-30 March.

[14] Kim S.H., Kim Y., Yoon Y.J., 2015. Reflectarray element combined a tripole with double rings and broadband RCS reduction. International Workshop on Antenna Technology (iWAT), Seoul, South Korea, 4-6 March.

[15] Bodur H., Ünalı S., Çimen S., Çakır G., 2016. X-Bant uygulamalar için tek katmanlı geniş bant yansıtıcı dizi anten tasarımı. Paper presented at URSI-TÜRKİYE'2016 VIII. Bilimsel Kongresi, Ankara, Turkey, 1-3 September.



## A Characterization of Factorable Surfaces in Euclidean 4-Space $\mathbb{IE}^4$

Sezgin Büyükkütük<sup>1,\*</sup> and Günay Öztürk<sup>1</sup>

<sup>1</sup>Department of Mathematics, Art and Science Faculty, Kocaeli, 41380, Turkey

### Article Info

#### Research paper

Received : 09/03/2018

Accepted : 21/04/2018

### Keywords

Curvature ellipse  
Factorable surface  
Gaussian curvature  
Mean curvature  
Normal curvature  
Wintgen ideal surface

### Abstract

In this paper, we consider a factorable surface in Euclidean space  $\mathbb{IE}^4$  with its curvature ellipse. We classify the origin of the normal space of such a surface according to whether it is hyperbolic, parabolic, or elliptic. Further, we give the necessary and sufficient condition of the factorable surface to become Wintgen ideal surface.

## 1. Introduction

Let  $S$  be a smooth surface given with the patch  $X(u, v) : (u, v) \in D \subset \mathbb{IE}^2$  in  $\mathbb{IE}^4$ . The tangent space to  $S$  at an arbitrary point  $p = X(u, v)$  of  $S$  is spanned  $\{X_u, X_v\}$ . In the chart  $(u, v)$  the coefficients of first fundamental form of  $S$  are given by

$$E = \langle X_u, X_u \rangle, F = \langle X_u, X_v \rangle, G = \langle X_v, X_v \rangle,$$

where  $\langle \cdot, \cdot \rangle$  is the Euclidean inner product. We assume that

$W^2 = EG - F^2 \neq 0$ , i.e. the surface patch  $X(u, v)$  is regular. For each  $p \in S$ , it is considered the decomposition

$T_p \mathbb{IE}^4 = T_p S \oplus T_p^\perp S$  where  $T_p^\perp S$  is the orthogonal component of  $T_p S$  in  $\mathbb{IE}^4$ .

Let  $\chi(S)$  and  $\chi^\perp(S)$  be the spaces of smooth vector fields tangent to  $S$  and normal to  $S$ , respectively. Given any local

vector fields  $X_1, X_2$  tangent to  $S$ , it is considered the second fundamental map  $h : \chi(S) \times \chi(S) \rightarrow \chi^\perp(S)$ ;

$$h(X_i, X_j) = \tilde{\nabla}_{X_i} X_j - \nabla_{X_i} X_j, \quad 1 \leq i, j \leq 2 \quad (1)$$

where  $\nabla$  and  $\tilde{\nabla}$  are the induced connection of  $S$  and the Riemannian connection of  $\mathbb{IE}^4$ , respectively. This map is well-defined, symmetric and bilinear [1].

For any arbitrary orthonormal frame field  $\{N_1, N_2\}$  of  $S$ , recall the shape operator  $A : \chi^\perp(S) \times \chi(S) \rightarrow \chi(S)$ ;

$$A_{N_k} X_j = -(\tilde{\nabla}_{X_j} N_k)^T, \quad X_j \in \chi(S) \quad k = 1, 2.$$

This operator is bilinear, self-adjoint and satisfies the following equation:

$$\begin{aligned} \langle A_{N_k} X_j, X_i \rangle &= \langle h(X_i, X_j), N_k \rangle \\ &= c_{ij}^k, \quad 1 \leq i, j, k \leq 2, \end{aligned} \quad (2)$$

\* Corresponding Author: sezginbuyukkutuk@kocaeli.edu.tr

where  $c_{ij}^k$  are the coefficients of the second fundamental form [2].

The coefficients of the second fundamental form for a surface  $S: X(u, v)$  in  $IE^n$  can be calculated by

$$\begin{aligned} c_{11}^k &= \langle X_{uu}, N_k \rangle, \\ c_{12}^k &= \langle X_{uv}, N_k \rangle, \quad 1 \leq k \leq n-2 \\ c_{22}^k &= \langle X_{vv}, N_k \rangle \end{aligned} \tag{3}$$

where  $X_{uu} = \tilde{\nabla}_{X_u} X_u$ ,  $X_{uv} = \tilde{\nabla}_{X_u} X_v$ ,  $X_{vv} = \tilde{\nabla}_{X_v} X_v$ .

Eq. (1) is called Gaussian formula, and

$$h(X_i, X_j) = \sum_{k=1}^2 c_{ij}^k N_k, \quad 1 \leq i, j \leq 2. \tag{4}$$

Then, the Gaussian curvature and Gaussian torsion of a regular patch  $X(u, v)$  are given by

$$K = \frac{1}{W^2} \sum_{k=1}^2 (c_{11}^k c_{22}^k - (c_{12}^k)^2) \tag{5}$$

and

$$K_N = \frac{1}{W^2} \begin{pmatrix} E(c_{12}^1 c_{22}^2 - c_{12}^2 c_{22}^1) \\ -F(c_{11}^1 c_{22}^2 - c_{11}^2 c_{22}^1) \\ +G(c_{11}^1 c_{12}^2 - c_{11}^2 c_{12}^1) \end{pmatrix} \tag{6}$$

,respectively.

Further, the mean curvature vector of a regular patch  $X(u, v)$  is given by

$$H = \frac{1}{2W^2} \sum_{k=1}^2 (c_{11}^k G + c_{22}^k E - 2c_{12}^k F) N_k. \tag{7}$$

The norm of the mean curvature vector  $\|H\|$  is called the mean curvature of  $S$ .

A surface  $S$  is called a Wintgen ideal surface if it satisfies the equation  $K + |K_N| = \|H\|^2$  [3]. This condition is related by the notion of curvature ellipse of a surface. Curvature ellipses of some surfaces and especially Wintgen ideal surfaces are investigated in studies [3, 4, 5, 6, 7, 8, 9].

Factorable surfaces (also known homothetical surfaces) can be parametrized, locally, as  $X(u, v) = (u, v, f(u)g(v))$ , where  $f$  and  $g$  smooth functions [10, 11]. Some authors have considered factorable

surfaces in Euclidean and semi-Euclidean spaces [11, 12, 13, 14]. In [10], Van de Woestyne proved that the only minimal factorable non-degenerate surfaces in  $IL^3$  are planes and helicoids. Recently, the authors have studied spacelike factorable surfaces in four dimensional Minkowski space [15].

In the present study, we consider a factorable surface which locally can be written as a monge patch

$$X(u, v) = (u, v, f_1(u)g_1(v), f_2(u)g_2(v)),$$

for some differentiable functions,  $f_i(u), g_i(v), i = 1, 2$  [16, 17]. We characterize the factorable surfaces in Euclidean 4-space with regards to their curvature ellipses. We classify the origin of normal space of a surface according to whether it is hyperbolic, parabolic, or elliptic. Further, we calculate Gaussian curvature, the normal curvature and mean curvature of the surface and give the necessary and sufficient condition for the factorable surfaces to become Wintgen ideal surface.

## 2. The Notion of Curvature Ellipse

Let  $S \subset IE^4$  be a surface given with the regular patch  $X(u, v)$  and consider a circle with the parameter  $\theta \in [0, 2\pi]$  in the tangent space  $T_p S$  on the point  $p$ . Let the curve  $\gamma(\theta)$  indicate the intersection of the surface  $S$  and the hyperplane which is the direct sum of the normal plane on the point  $p$  and the tangent vector

$$X = \cos\theta X_1 + \sin\theta X_2$$

where  $X_1, X_2$  are orthonormal base of  $T_p S$ . This curve is called normal section curve of  $S$  on  $p$  in the direction  $X$ . Additionally, the normal curvature vector  $\eta_\theta$  is a vector that lies on the normal plane. Varying  $\theta$  from 0 to  $2\pi$ , this vector defines an ellipse on normal plane. This ellipse is called as curvature ellipse of  $S$  on  $p$ . Thus; the curvature ellipse of  $S$  on  $p$  is defined by

$$E(p) = \{h(X, X) : X \in T_p S, \|X\| = 1\} \tag{8}$$

where  $\gamma'_\theta = X = \cos\theta X_1 + \sin\theta X_2$  is the unit tangent vector of normal section curve and  $h$  is the second fundamental form of the patch  $X(u, v)$ . The reason why the Eq. (8) indicates an ellipse is that the second fundamental form satisfies the relation

$$h(X, X) = H + \cos \theta B + \sin \theta C,$$

where

$$B = \frac{1}{2}(h(X_1, X_1) + h(X_2, X_2)), C = h(X_1, X_2)$$

are normal vectors and  $H$  is the mean curvature vector of  $S$ . While the unit vector  $X$  makes one turn around the unit circle, the vector  $h(X, X)$  takes two turns around the ellipse centered at  $H$ . It is possible that the ellipse  $E(p)$  can degenerate into a point or a straight line.

Definition 1. Let  $S \subset \mathbb{E}^4$  be a surface given with the regular patch  $X(u, v)$ . If the condition

$$\langle B, C \rangle = 0 \text{ and } \|B\| = \|C\|$$

is satisfied, then the curvature ellipse of  $S$  is congruent to a circle.

Remark 1. The curvature ellipse is congruent to a circle if and only if

$$\|H\|^2 - K - |K_N| = 0$$

is hold. The surface is called superconformal if its curvature ellipse is congruent to a circle. Thus, Wintgen ideal surfaces are superconformal at the same time.

Definition 2. Let  $S \subset \mathbb{E}^4$  be a surface given with the regular patch  $X(u, v)$ . The determinant  $\Delta(p)$  and the matrix  $\alpha(p)$  are defined by

$$\Delta(p) = \frac{1}{W^2} \det \begin{pmatrix} c_{11}^1 & 2c_{12}^1 & c_{22}^1 & 0 \\ c_{11}^2 & 2c_{12}^2 & c_{22}^2 & 0 \\ 0 & c_{11}^1 & 2c_{12}^1 & c_{22}^1 \\ 0 & c_{11}^2 & 2c_{12}^2 & c_{22}^2 \end{pmatrix} (p) \quad (9)$$

and

$$\alpha(p) = \begin{pmatrix} c_{11}^1 & 2c_{12}^1 & c_{22}^1 \\ c_{11}^2 & c_{12}^2 & c_{22}^2 \end{pmatrix} (p) \quad (10)$$

where  $c_{ij}^k$ , ( $i, j, k = 1, 2$ ) are the coefficients of the second fundamental form of  $S$  [18].

The following classification can be given for the origin  $p$  of the normal space  $T_p^\perp S$ :

(i) If  $\Delta(p) < 0$ , then the point  $p$  is outside the curvature ellipse  $E(p)$  and is called hyperbolic point.

(ii) If  $\Delta(p) = 0$ , then the point  $p$  is on the curvature ellipse  $E(p)$  and is called parabolic point. According to this

(a) If  $\Delta(p) = 0$  and  $K(p) > 0$ , then the point  $p$  is an inflection point of imaginary type.

(b) If  $\Delta(p) = 0$  and  $K(p) < 0$ , then

$\text{rank } \alpha(p) = 2 \Rightarrow$  the point  $p$  is non-degenerate.

$\text{rank } \alpha(p) = 1 \Rightarrow$  the point  $p$  is an inflection point of real type.

(c) If  $\Delta(p) = 0$  and  $K(p) = 0$ , then the point  $p$  is an inflection point of real type.

(iii) If  $\Delta(p) > 0$ , then the point  $p$  is inside the curvature ellipse  $E(p)$  and is called elliptic point.

### 3. Factorable Surfaces in $\mathbb{E}^4$

Definition 3. Let  $S$  be a surface in 4-dimensional Euclidean space  $\mathbb{E}^4$ . If the surface is given by an explicit form  $z(u, v) = f_1(u)g_1(v)$  and  $w(u, v) = f_2(u)g_2(v)$  where  $u, v, z, w$  are Cartesian coordinates in  $\mathbb{E}^4$  and  $f_i, g_i, i \in \{1, 2\}$  are smooth functions, then the surface is called a factorable surface in  $\mathbb{E}^4$ . Thus, the factorable surface can be written as a monge patch

$$X(u, v) = (u, v, f_1(u)g_1(v), f_2(u)g_2(v)). \quad (11)$$

Let  $S$  be a factorable surface with the parametrization Eq. (11). Then, we have the following:

The tangent space of  $S$  is spanned by the vector fields

$$X_u = (1, 0, f_1'(u)g_1(v), f_2'(u)g_2(v)),$$

$$X_v = (0, 1, f_1(u)g_1'(v), f_2(u)g_2'(v)).$$

Hence, the coefficients of the first fundamental form of the surface are

$$E = \langle X_u, X_u \rangle = 1 + (f_1'g_1)^2 + (f_2'g_2)^2$$

$$F = \langle X_u, X_v \rangle = f_1'f_1g_1'g_1 + f_2'f_2g_2'g_2 \quad (12)$$

$$G = \langle X_v, X_v \rangle = 1 + (f_1g_1')^2 + (f_2g_2')^2$$

where  $\langle \cdot, \cdot \rangle$  is standard scalar product in  $\mathbb{E}^4$ . Since the surface  $S$  is non-degenerate, then

$\|X_u \times X_v\| = \sqrt{EG - F^2} \neq 0$ . For the later use we define a smooth function  $W$  as  $W = \|X_u \times X_v\|$ .

The second partial derivatives of  $X(u, v)$  are expressed as follows;

$$\begin{aligned} X_{uu} &= (0, 0, f_1''(u)g_1(v), f_2''(u)g_2(v)), \\ X_{uv} &= (0, 0, f_1'(u)g_1'(v), f_2'(u)g_2'(v)), \\ X_{vv} &= (0, 0, f_1(u)g_1''(v), f_2(u)g_2''(v)). \end{aligned} \tag{13}$$

Further, the normal space of  $S$  is spanned by the orthonormal vector fields

$$N_1 = \frac{1}{\sqrt{\tilde{E}}} (-f_1'(u)g_1(v), -f_1(u)g_1'(v), 1, 0), \tag{14}$$

$$N_2 = \frac{1}{\sqrt{\tilde{E}W}} \begin{pmatrix} \tilde{F}f_1'(u)g_1(v) - \tilde{E}f_2'(u)g_2(v), \\ \tilde{F}f_1(u)g_1'(v) - \tilde{E}f_2(u)g_2'(v), \\ -\tilde{F}, \tilde{E} \end{pmatrix}$$

where

$$\begin{aligned} \tilde{E} &= 1 + (f_1'g_1)^2 + (f_1g_1')^2, \\ \tilde{F} &= f_1'f_2'g_1g_2 + f_1f_2g_1'g_2', \\ \tilde{G} &= 1 + (f_2'g_2)^2 + (f_2g_2')^2. \end{aligned} \tag{15}$$

Also,  $\tilde{E}\tilde{G} - \tilde{F}^2 = W^2$ . Using Eq. (13) and Eq. (14), we can calculate the coefficients of the second fundamental form as follows;

$$\begin{aligned} c_{11}^1 &= \frac{f_1''g_1}{\sqrt{\tilde{E}}}, & c_{22}^1 &= \frac{f_1g_1''}{\sqrt{\tilde{E}}}, \\ c_{12}^1 &= \frac{f_1'g_1'}{\sqrt{\tilde{E}}}, & c_{12}^2 &= \frac{\tilde{E}f_2'g_2' - \tilde{F}f_1'g_1'}{\sqrt{\tilde{E}W}}, \\ c_{11}^2 &= \frac{\tilde{E}f_2''g_2 - \tilde{F}f_1''g_1}{\sqrt{\tilde{E}W}}, \\ c_{22}^2 &= \frac{\tilde{E}f_2g_2'' - \tilde{F}f_1g_1''}{\sqrt{\tilde{E}W}}. \end{aligned} \tag{16}$$

### 3.1. Curvature Ellipse of the Factorable Surface

**Theorem 1** Let  $S$  be a factorable surface given with the parametrization Eq. (11) in Euclidean 4-space  $\mathbb{E}^4$ . Then the origin  $p$  of  $T_p^\perp S$  can be characterized by the followings:

(i) If

$$\begin{aligned} &4(f_1''g_1f_2'g_2' - f_2''g_2f_1'g_1')(f_2g_2''f_1'g_1' - f_1g_1''f_2'g_2') \\ &= (f_1''g_1f_2g_2'' - f_1g_1''f_2''g_2)^2 \end{aligned} \tag{17}$$

is hold, then the point  $p$  is on the curvature ellipse. This point is the parabolic point of  $S$ .

(ii) If

$$\begin{aligned} &4(f_1''g_1f_2'g_2' - f_2''g_2f_1'g_1')(f_2g_2''f_1'g_1' - f_1g_1''f_2'g_2') \\ &< (f_1''g_1f_2g_2'' - f_1g_1''f_2''g_2)^2 \end{aligned} \tag{18}$$

is hold, then the point  $p$  is outside the curvature ellipse. This point is the hyperbolic point of  $S$ .

(iii) If

$$\begin{aligned} &4(f_1''g_1f_2'g_2' - f_2''g_2f_1'g_1')(f_2g_2''f_1'g_1' - f_1g_1''f_2'g_2') \\ &> (f_1''g_1f_2g_2'' - f_1g_1''f_2''g_2)^2 \end{aligned} \tag{19}$$

is hold, then the point  $p$  is inside the curvature ellipse. This point is the elliptic point of  $S$ .

**Proof.** Let  $S$  be a factorable surface given with the parametrization Eq. (11) in Euclidean 4-space  $\mathbb{E}^4$ . By the use of the Equation (9) and the second fundamental form coefficients, we get

$$\Delta(p) = \frac{\begin{bmatrix} 4(f_1''g_1f_2'g_2' - f_2''g_2f_1'g_1')(f_2g_2''f_1'g_1' - f_1g_1''f_2'g_2') \\ - (f_1''g_1f_2g_2'' - f_1g_1''f_2''g_2)^2 \end{bmatrix}}{4W^2}$$

With the help of the Definition 2, if  $\Delta(p) < 0$ , then the point  $p$  is outside the curvature ellipse. If  $\Delta(p) > 0$ , then the point  $p$  is outside the curvature ellipse. If  $\Delta(p) = 0$ , then the point  $p$  is on the curvature ellipse. Thus, desired result is obtained.

**Example 1.** Let  $S$  be a factorable surface given with the parametrization Eq. (11) in Euclidean 4-space  $\mathbb{E}^4$ . If the functions are choosen as:

$$\begin{aligned} f_1(u) &= 3u + 1, & g_1(v) &= \cos v, \\ f_2(u) &= 2u + 2, & g_2(v) &= \sin v, \end{aligned} \tag{20}$$

then the origin  $p$  of  $T_p^\perp S$  is on the curvature ellipse.  $p$  is parabolic point. Also, projection of the surface onto  $\mathbb{E}^3$  is given in Figure 1.

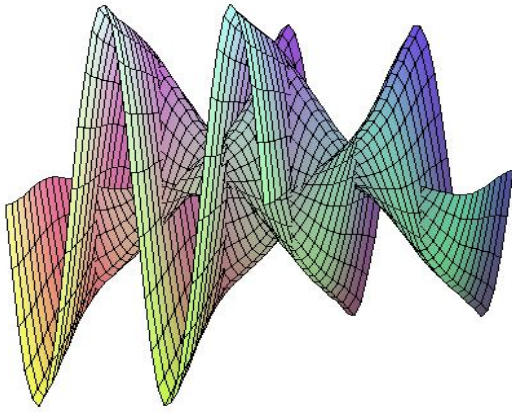


**Figure 1.** A Factorable Surface Given by the Functions in Eq. (20)

### 3.2. Wintgen Ideal Surface

In 1979, P. Wintgen [3] proved a basic relationship between the Gaussian curvature  $K$ , normal curvature  $K_N$ , and the mean curvature  $H$  of a surface  $S$  in Euclidean 4-space  $IE^4$  that is

$$K + |K_N| \leq \|H\|^2. \tag{21}$$

The equality is hold if and only if the curvature ellipse is a circle.

Definition 4. A surface  $S$  in  $IE^4$  is called a Wintgen ideal surface if it satisfies the equality case in the inequality (21), namely

$$K + |K_N| = \|H\|^2. \tag{22}$$

Theorem 2. Let  $S$  be a factorable surface given with the parameterization (11) in Euclidean 4-space  $IE^4$ . Then the Gaussian curvature of  $S$  is

$$K = \frac{\begin{bmatrix} (f_1'' f_1 g_1'' g_1 - f_1'^2 g_1'^2) \tilde{G} \\ -(f_1'' f_2 g_1 g_2'' + f_1 f_2'' g_1'' g_2 - 2f_1' f_2' g_1' g_2') \tilde{F} \\ + (f_2'' f_2 g_2'' g_2 - f_2'^2 g_2'^2) \tilde{E} \end{bmatrix}}{W^4} \tag{23}$$

where  $\tilde{E}$ ,  $\tilde{F}$ , and  $\tilde{G}$  are given by the Equation (15).

Proof. Let  $S$  be a factorable surface in  $IE^4$ . Substituting the second fundamental form coefficients of  $S$  into the Eq. (5), we obtain the desired result.

Theorem 3. Let  $S$  be a factorable surface given with the

parameterization Eq. (11) in Euclidean 4-space  $IE^4$ . Then the normal curvature function of  $S$  is

$$K_N = \frac{\begin{bmatrix} E(f_1' f_2 g_1' g_2'' - f_1 f_2' g_1'' g_2') \\ -F(f_1'' f_2 g_1 g_2'' - f_1 f_2'' g_1'' g_2) \\ +G(f_1'' f_2' g_1 g_2' - f_1' f_2'' g_1' g_2) \end{bmatrix}}{W^4} \tag{24}$$

where  $E, F,$  and  $G$  are the first fundamental form coefficients which are given by Eq. (12).

Proof. Let  $S$  be a factorable surface in  $IE^4$ . Substituting the second fundamental form coefficients of  $S$  into the Eq. (6), we obtain the desired result.

Theorem 4. Let  $S$  be a factorable surface given with the parameterization Eq. (11) in Euclidean 4-space  $IE^4$ . Then the mean curvature of  $S$  is

$$H = \frac{f_1'' g_1 G + f_1 g_1'' E - 2f_1' g_1' F}{2\sqrt{\tilde{E}} W^2} N_1 + \frac{\begin{bmatrix} \tilde{E}(f_2'' g_2 G + f_2 g_2'' E - 2f_2' g_2' F) \\ -\tilde{F}(f_1'' g_1 G + f_1 g_1'' E - 2f_1' g_1' F) \end{bmatrix}}{2\sqrt{\tilde{E}} W^3} N_2. \tag{25}$$

Proof. Let  $S$  be a factorable surface in  $IE^4$ . Substituting the second fundamental form coefficients of  $S$  into the Eq. (7), we obtain the desired result.

Theorem 5. Let  $S$  be a factorable surface given with the parameterization Eq. (11) in  $IE^4$ . Then the surface is Wintgen ideal (superconformal) surface if and only if

$$\begin{aligned} & \tilde{G} \left[ (f_1'' g_1 G + f_1 g_1'' E - 2f_1' g_1' F) - 4W^2 (f_1'' f_1 g_1'' g_1 - f_1'^2 g_1'^2) \right] \\ & + \tilde{E} \left[ (f_2'' g_2 G + f_2 g_2'' E - 2f_2' g_2' F) \right. \\ & \quad \left. - 4W^2 (f_2'' f_2 g_2'' g_2 - f_2'^2 g_2'^2) \right] \\ & - 2\tilde{F} \left[ (f_1'' g_1 G + f_1 g_1'' E - 2f_1' g_1' F) \right. \\ & \quad \left. (f_2'' g_2 G + f_2 g_2'' E - 2f_2' g_2' F) \right. \\ & \quad \left. - 2W^2 (f_1'' f_2 g_1 g_2'' + f_1 f_2'' g_1'' g_2 - 2f_1' f_2' g_1' g_2') \right] \\ & = \pm 4W^2 \begin{bmatrix} E(f_1' f_2 g_1' g_2'' - f_1 f_2' g_1'' g_2') \\ -F(f_1'' f_2 g_1 g_2'' - f_1 f_2'' g_1'' g_2) \\ +G(f_1'' f_2' g_1 g_2' - f_1' f_2'' g_1' g_2) \end{bmatrix} \end{aligned}$$

is hold.

Proof. Let  $S$  be a factorable surface given with the

parameterization Eq. (11) in  $\mathbb{E}^4$ . Substituting Eq. (23), (24), and (25) into the relation (22), we obtain the desired result.

Example 2. The plane given with the parameterization

$$X(u, v) = (u, v, c_1v + c_2, c_3u + c_4) \quad (26)$$

is obviously a Wintgen ideal and factorable surface in  $\mathbb{E}^4$  where  $f_1(u) = 1$ ,  $g_2(v) = 1$ , and  $c_i, i = 1, \dots, 4$  are real constants.

## References

- [1] Chen B. Y., 1973. Geometry of Submanifolds. Marcel Dekker, New York.
- [2] Gutierrez Nunez J.M., Romero Fuster M.C., Sanchez-Bringas F., 2008. Codazzi fields on surfaces immersed in Euclidean 4 – spaces. Osaka J. Math **45**, 877–894.
- [3] Wintgen P., 1979. Sur l'inegalite de Chen-Wilmore. C. R. Acad. Sci., Paris, **288**, 993–995.
- [4] Arslan K., Bayram B.K., Bulca B., Öztürk G., 2012. Generalized rotation surfaces in  $\mathbb{E}^4$ . Results in Mathematics **61**, 315–327.
- [5] Bayram B.K., Bulca B., Arslan K., Öztürk G., 2009. Superconformal ruled surfaces in  $\mathbb{E}^4$ . Math. Commun. **14**, 235–244.
- [6] Bulca B., Arslan K., 2014. Semiparallel Wintgen ideal surfaces in  $\mathbb{E}^n$ . C. R. Acad. Bulgare Sci. **67**, 613–622.
- [7] Bulca B., Arslan K., Bayram B.K., Öztürk G., 2012. Spherical product surface in  $\mathbb{E}^4$ . An. St. Univ. Ovidius Constanta **20**, 41–54.
- [8] Chen B. Y., 2011. On Wintgen ideal surfaces, Proceedings of The Conference RIGA 2011, Riemannian Geometry and Applications, Bucharest, Romania, 10-14 May 2011, 59–74.
- [9] İyigün E., Arslan K., Öztürk G., 2018. A characterization of Chen surfaces in  $\mathbb{E}^4$ . Bull. Malays. Math. Math. Soc. **31**, 209–215.
- [10] Woestyne I. V., 1993. A new characterization of helicoids. Geometry and topology submanifolds World Sci. Publ. River Edge, 267–273.
- [11] Woestyne I. V., 1995. Minimal homothetical hypersurfaces of a semi-Euclidean space. Results Math. **27**, 333–342.
- [12] Lopez R., Moruz M., 2015. Translation and homothetical surfaces in Euclidean spaces with constant curvature. J. Korean Math. Soc. **52**, 523–535.
- [13] Meng H., Liu H. 2009. Factorable surfaces in 3 – Minkowski space. Bull. Korean Math. Soc. **46**, 155–169.
- [14] Yu Y., Liu H., 2007. The factorable minimal surfaces. Proceedings of the Eleventh International Workshop on Diff. Geom. **11**, 33–39.
- [15] Büyükkütük S., Öztürk G., 2017. Spacelike factorable surfaces in four-dimensional Minkowski space. Bulletin of Mathematical Analysis and Applications **9**, 12–20.
- [16] Aminov Y. A., 1994. Surfaces in  $\mathbb{E}^4$  with a Gaussian curvature coinciding with a Gaussian torsion up to sign. Mathematical Notes **56**, 5–6.
- [17] Bulca B., Arslan K., 2013. Surfaces given with the Monge patch in  $\mathbb{E}^4$ . Journal of Mathematical Physics, Analysis, Geometry **9**, 435–447.
- [18] Little J.A., 1969. On singularities of submanifolds of higher dimensional Euclidean space. Ann. Math. Pura Appl. (Ser. 4A) **83**, 261–335.

